





# Active–Sterile Neutrino Oscillations in Neutrino-driven Winds: Implications for Nucleosynthesis

Zewei Xiong<sup>1</sup> , Meng-Ru Wu<sup>2,3</sup>, and Yong-Zhong Qian<sup>1,4</sup> <sup>1</sup> School of Physics and Astronomy, University of Minnesota, Minneapolis, MN 55455, USA<sup>2</sup> Institute of Physics, Academia Sinica, Taipei 11529, Taiwan<sup>3</sup> Institute of Astronomy and Astrophysics, Academia Sinica, Taipei 10617, Taiwan<sup>4</sup> Tsung-Dao Lee Institute, Shanghai 200240, People's Republic of China

Received 2019 April 19; revised 2019 June 7; accepted 2019 June 7; published 2019 July 29

## Abstract

A protoneutron star produced in a core-collapse supernova (CCSN) drives a wind by its intense neutrino emission. We implement active–sterile neutrino oscillations in a steady-state model of this neutrino-driven wind to study their effects on the dynamics and nucleosynthesis of the wind in a self-consistent manner. Using vacuum mixing parameters indicated by some experiments for a sterile  $\nu_s$  of  $\sim 1$  eV in mass, we observe interesting features of oscillations due to various feedback. For the higher  $\nu_s$  mass values, we find that oscillations can reduce the mass-loss rate and the wind velocity by a factor of  $\sim 1.6$ – $2.7$  and change the electron fraction critical to nucleosynthesis by a significant to large amount. In the most dramatic cases, oscillations shift nucleosynthesis from dominant production of  $^{45}\text{Sc}$  to that of  $^{86}\text{Kr}$  and  $^{90}\text{Zr}$  during the early epochs of the CCSN evolution.

*Key words:* neutrinos – nuclear reactions, nucleosynthesis, abundances – stars: mass-loss – stars: neutron – supernovae: general

## 1. Introduction

In this paper we study the effects of active–sterile neutrino oscillations on the dynamics and nucleosynthesis of neutrino-driven winds. The protoneutron star (PNS) formed in a core-collapse supernova (CCSN) is a profuse source of  $\nu_e$ ,  $\bar{\nu}_e$ ,  $\nu_\mu$ ,  $\bar{\nu}_\mu$ ,  $\nu_\tau$ , and  $\bar{\nu}_\tau$ . These neutrinos interact with the material in the vicinity of the PNS mainly through

$$\nu_e + n \rightarrow p + e^-, \quad (1a)$$

$$\bar{\nu}_e + p \rightarrow n + e^+. \quad (1b)$$

This heating drives a wind (Duncan et al. 1986), which eventually becomes part of the ejecta from the CCSN. This neutrino-driven wind has been studied extensively as a site for production of elements heavier than the Fe group (Meyer et al. 1992; Woosley & Baron 1992; Woosley & Hoffman 1992; Takahashi et al. 1994; Wittl et al. 1994; Woosley et al. 1994; Qian & Woosley 1996; Hoffman et al. 1997; Thompson et al. 2001; Wanajo et al. 2001; Roberts et al. 2010; Wanajo 2013). The neutrino reactions in Equations 1(a) and 1(b) not only provide the heating, but also determine the neutron-to-proton ratio of the wind (Qian et al. 1993; Qian & Woosley 1996). This ratio is equivalent to the net number of electrons per baryon, i.e., the electron fraction  $Y_e$ , and is a critical parameter for nucleosynthesis. Because neutrinos of different flavors interact differently with matter, neutrino flavor oscillations would potentially impact the dynamics and nucleosynthesis of the wind (e.g., Qian et al. 1993). Here we focus on the oscillations between  $\nu_e$  ( $\bar{\nu}_e$ ) and  $\nu_s$  ( $\bar{\nu}_s$ ), where  $\nu_s$  ( $\bar{\nu}_s$ ) is a sterile species that does not have normal weak interaction like an active one.

The existence of sterile neutrinos have been discussed based on both theoretical and experimental considerations (e.g., Abazajian et al. 2012). Potential effects of active–sterile neutrino oscillations on the dynamics and nucleosynthesis of

CCSNe have also been studied (e.g., Nunokawa et al. 1997; McLaughlin et al. 1999; Tamborra et al. 2012; Wu et al. 2014; Pllumbi et al. 2015). These previous studies, however, are not fully self-consistent in that they did not take into account the feedback of active–sterile neutrino oscillations on the velocity ( $v$ ), density ( $\rho$ ), and temperature ( $T$ ) profiles of the CCSN. In this paper we make a significant step toward treating such feedback by coupling neutrino flavor evolution with the evolution of  $v$ ,  $\rho$ ,  $T$ , and  $Y_e$  in the neutrino-driven wind.

This paper is organized as follows. In Section 2, we describe our steady-state model of the neutrino-driven wind including active–sterile neutrino oscillations. In Section 3, we present the results for nine cases that correspond to winds ejected at three representative times of CCSN evolution with three different sets of neutrino oscillation parameters. For each case, we show the profiles of  $v$ ,  $\rho$ ,  $T$ , and  $Y_e$  in the wind and compare them with those in the absence of oscillations. In Section 4, we show the effects of active–sterile neutrino oscillations on nucleosynthesis in the wind. We summarize our results and give conclusions in Section 5.

## 2. Model of the Neutrino-driven Wind

A massive star arrives at the end of its life when nuclear fuel is exhausted in its core. The core undergoes gravitational collapse and bounces when supranuclear density is reached at the center and a PNS is born. The bounce launches a shock, which is stalled on the way out of the core due to energy loss from dissociating nuclei into mostly free nucleons. How this shock is revived to make an explosion is the crux of the CCSN mechanism (e.g., Janka 2012). Neutrinos emitted by the PNS are thought to play a critical role by heating the material behind the stalled shock mainly through the reactions in Equations 1(a) and 1(b) (Bethe & Wilson 1985). Because the neutrino emission lasts for  $\sim 10$  s, the same heating continues to drive a mass outflow, the so-called neutrino-driven wind, after the shock is revived.

While the wind can be studied within a CCSN simulation, its physical conditions can be understood quite well by treating it as a stationary mass outflow between the PNS and the shock (Qian & Woosley 1996). In the latter approach, the wind is the solution to an eigenvalue problem with the inner and outer boundaries specified by the PNS and shock, respectively. The eigenvalue to be determined is the mass-loss rate  $\dot{M}$ . We will take this approach in this paper. The inner boundary is specified by the radius  $R_\nu$  of the PNS, which also defines the surface of neutrino emission, or the neutrinosphere. On the timescale for a mass element in the wind to receive significant neutrino heating, the neutrino luminosities and energy spectra at emission stay approximately fixed. Therefore, the wind can be considered as a steady-state configuration obtained for a PNS with a fixed  $R_\nu$  and a fixed mass  $M_{\text{PNS}}$  that emits neutrinos with fixed luminosities and energy spectra.

### 2.1. Equations for the Wind

In this paper we ignore the effects of general relativity. To good approximation,  $v$  is nonrelativistic and the internal energy of a mass element in the wind is much smaller than its rest-mass energy. Based on the above considerations, the equations describing a spherically symmetric steady-state wind (e.g., Qian & Woosley 1996) are

$$4\pi r^2 \rho v = \dot{M}, \quad (2a)$$

$$v \frac{dv}{dr} = -\frac{1}{\rho} \frac{dP}{dr} - \frac{GM_{\text{PNS}}}{r^2}, \quad (2b)$$

$$\frac{d\epsilon}{dr} - \frac{P}{\rho^2} \frac{d\rho}{dr} = \frac{\dot{q}}{v}, \quad (2c)$$

$$\frac{dY_e}{dr} = \frac{1}{v} [(\lambda_{\nu_e n} + \lambda_{e^+ n}) Y_n - (\lambda_{\bar{\nu}_e p} + \lambda_{e^- p}) Y_p], \quad (2d)$$

where  $P$  is the pressure,  $G$  is the gravitational constant,  $\epsilon$  is the internal energy per unit mass,  $\dot{q}$  is the rate of net energy gain per unit mass,  $Y_n$  ( $Y_p$ ) is the number of free neutrons (protons) per baryon, i.e., the number fraction of free neutrons (protons), and  $\lambda_{\nu_e n}$  ( $\lambda_{e^- p}$ ) and  $\lambda_{\bar{\nu}_e p}$  ( $\lambda_{e^+ n}$ ) are the rates per target nucleon for the reactions (inverse reactions) in Equations 1(a) and (b), respectively.

The equation of state determines  $P$  and  $\epsilon$  as functions of  $\rho$ ,  $T$ , and the composition of the wind. We assume that the wind is electrically neutral and composed of neutrons, protons,  $\alpha$ -particles, electrons, positrons, and photons. We further assume nuclear statistical equilibrium (NSE) to determine the number fractions of the nuclear components,  $Y_n$ ,  $Y_p$ , and  $Y_\alpha$ :

$$Y_n + Y_p + 4Y_\alpha = 1, \quad (3a)$$

$$Y_p + 2Y_\alpha = Y_e, \quad (3b)$$

$$Y_\alpha = \frac{1}{2} Y_n^2 Y_p^2 \left( \frac{\rho}{m_u} \right)^3 \left( \frac{2\pi}{m_u T} \right)^{9/2} \exp\left( \frac{B_\alpha}{T} \right), \quad (3c)$$

where  $m_u$  is the atomic mass unit and  $B_\alpha \approx 28.3$  MeV is the nuclear binding energy of the  $\alpha$ -particle. We use the equation of state from Timmes & Arnett (1999) and Timmes & Swesty (2000) with the above composition. Note that in Equation 3(c) and hereafter, the speed of light  $c$ , the Planck constant  $\hbar$ , and the Boltzmann constant  $k$  are set to unity.

Given the inner and outer boundary conditions at the PNS and the shock, respectively, the eigenvalue  $\dot{M}$  can be

determined by solving the wind equations once the rates  $\dot{q}$ ,  $\lambda_{\nu_e n}$ ,  $\lambda_{e^+ n}$ ,  $\lambda_{\bar{\nu}_e p}$ , and  $\lambda_{e^- p}$  are specified. In practice, we solve for  $v$ ,  $\rho$ ,  $T$ , and  $Y_e$  as functions of the radius  $r$ . The corresponding  $Y_n$ ,  $Y_p$ , and  $Y_\alpha$  are specified by NSE and the corresponding  $P$  and  $\epsilon$  are obtained from the equation of state.

### 2.2. Rates for Energy Gain or Loss and Neutron–Proton Interconversion

The rate of net energy gain per unit mass,  $\dot{q}$ , is

$$\begin{aligned} \dot{q} = & \dot{q}_\alpha + 2\dot{q}_{\nu_x n} + 2\dot{q}_{\bar{\nu}_x n} + 2\dot{q}_{\nu_x e^\pm} \\ & + 2\dot{q}_{\bar{\nu}_x e^\pm} + 2\dot{q}_{\nu_x \bar{\nu}_x} \\ & + \dot{q}_{\nu_e n} + \dot{q}_{\bar{\nu}_e p} + \dot{q}_{\nu_e n} + \dot{q}_{\bar{\nu}_e n} \\ & + \dot{q}_{\nu_e e^\pm} + \dot{q}_{\bar{\nu}_e e^\pm} + \dot{q}_{\nu_e \bar{\nu}_e} \\ & - \dot{q}_{e^+ n} - \dot{q}_{e^- p} - \dot{q}_{e^+ e^-}, \end{aligned} \quad (4)$$

where

$$\dot{q}_\alpha = v \left( \frac{dY_\alpha}{dr} \right) \frac{B_\alpha}{m_u} \quad (5)$$

corresponds to formation of  $\alpha$ -particles,  $\dot{q}_{\nu_x n}$  and  $\dot{q}_{\nu_x e^\pm}$  to scattering of  $\nu_x$  ( $\nu_\mu$  or  $\nu_\tau$ ) on nucleons and  $e^\pm$ , respectively,  $\dot{q}_{\nu_x \bar{\nu}_x}$  to  $\nu_x \bar{\nu}_x$  annihilation into  $e^\pm$ ,  $\dot{q}_{\nu_e n}$  ( $\dot{q}_{e^- p}$ ) and  $\dot{q}_{\bar{\nu}_e p}$  ( $\dot{q}_{e^+ n}$ ) to the reactions (inverse reactions) in Equations 1(a) and (b), respectively, and  $\dot{q}_{e^+ e^-}$  to  $e^\pm$  annihilation into neutrinos and antineutrinos of all three active flavors. The rates denoted by other subscripts are similar to those mentioned above. The factor of two associated with  $\nu_x(\bar{\nu}_x)$  assumes that  $\nu_\mu$  and  $\nu_\tau$  ( $\bar{\nu}_\mu$  and  $\bar{\nu}_\tau$ ) have identical emission characteristics.

Contributions to  $\dot{q}$ , as well as the rates  $\lambda_{\nu_e n}$ ,  $\lambda_{e^+ n}$ ,  $\lambda_{\bar{\nu}_e p}$ , and  $\lambda_{e^- p}$ , can be separated into those that are directly affected by active–sterile neutrino oscillations and those that are not. Those rates on the second line of Equation (4), as well as  $\lambda_{\nu_e n}$  and  $\lambda_{\bar{\nu}_e p}$ , belong to the former, while those on the first and last lines of Equation (4), as well as  $\lambda_{e^+ n}$  and  $\lambda_{e^- p}$ , belong to the latter. All of the rates are described in detail in the Appendix. Below we highlight those rates associated with neutrino interaction processes.

We assume that all neutrinos are emitted from a neutrinosphere of radius  $R_\nu$  with Fermi–Dirac spectra of zero chemical potential. For a specific neutrino species  $\nu_a$ , its normalized spectrum is

$$f_{\nu_a}(E) = \frac{1}{F_2(0) T_{\nu_a}^3} \frac{E^2}{\exp(E/T_{\nu_a}) + 1}, \quad (6)$$

where  $T_{\nu_a}$  is the temperature parameter characteristic of  $\nu_a$  emission. In the above equation,  $F_2(0)$  refers to the Fermi–Dirac integral defined as

$$F_k(y) = \int_0^\infty \frac{x^k}{\exp(x-y) + 1} dx. \quad (7)$$

At the neutrinosphere, the differential number density of  $\nu_a$  per unit energy interval per unit solid angle is

$$\left( \frac{d^2 n_{\nu_a}}{dE d\Omega} \right)_{R_\nu} = \frac{L_{\nu_a}}{4\pi^2 R_\nu^2 \langle E_{\nu_a} \rangle} f_{\nu_a}(E), \quad (8)$$

where  $L_{\nu_a}$  and  $\langle E_{\nu_a} \rangle = T_{\nu_a} F_3(0)/F_2(0)$  are the luminosity and average energy, respectively, of  $\nu_a$  at emission.

All neutrinos essentially free-stream above the neutrinosphere, but a small fraction can still interact, mostly with nucleons,  $e^\pm$ , and each other. The angle  $\theta$  between the neutrino's velocity and the radial direction at emission is related to the angle  $\theta_r$  defined in the same way at radius  $r$  by

$$\sin \theta_r = \frac{R_\nu}{r} \sin \theta. \quad (9)$$

Consequently, for an interaction point at radius  $r$ , only those neutrinos within the solid angle defined by polar angles  $0 \leq \theta_r \leq \theta_r^{\max}$  are relevant, where  $\theta_r^{\max}$  corresponds to a neutrino emitted tangentially at the neutrinosphere ( $\theta = \pi/2$ ) and satisfies

$$\sin \theta_r^{\max} = \frac{R_\nu}{r}. \quad (10)$$

Within this solid angle at radius  $r$ , the differential number density of  $\nu_a$  in the absence of neutrino oscillations is

$$\left( \frac{d^2 n_{\nu_a}}{dE d\Omega} \right)_r = \left( \frac{d^2 n_{\nu_a}}{dE d\Omega} \right)_{R_\nu}. \quad (11)$$

In the presence of active–sterile neutrino oscillations, the differential number density of active  $\nu_a$  at radius  $r$  is

$$\left( \frac{d^2 n_{\nu_a}}{dE d\Omega} \right)_r^{\text{osc}} = \left( \frac{d^2 n_{\nu_a}}{dE d\Omega} \right)_r P_{\nu_a}(E, r), \quad (12)$$

where  $P_{\nu_a}(E, r)$  is the probability for a  $\nu_a$  emitted with energy  $E$  to survive as a  $\nu_a$  at radius  $r$ .

As an example, we give the expression of  $\lambda_{\nu_e n}$  at radius  $r$  in the presence of active–sterile neutrino oscillations:

$$\lambda_{\nu_e n} = \int \left( \frac{d^2 n_{\nu_e}}{dE d\Omega} \right)_r^{\text{osc}} \sigma_{\nu_e n}(E) dE d\Omega_r \quad (13a)$$

$$= \frac{G_F^2 |V_{ud}|^2 (1 + 3g_A^2) L_{\nu_e} D(r)}{2\pi^2 R_\nu^2 \langle E_{\nu_e} \rangle} \int_0^\infty (E + \Delta)^2 \times \left( 1 - \frac{W_{\nu_e} E}{m_N} \right) f_{\nu_e}(E) P_{\nu_e}(E, r) dE, \quad (13b)$$

where

$$\sigma_{\nu_e n}(E) = \frac{G_F^2 |V_{ud}|^2 (1 + 3g_A^2)}{\pi} (E + \Delta)^2 \left( 1 - \frac{W_{\nu_e} E}{m_N} \right) \quad (14)$$

is the cross section for  $\nu_e$  absorption on neutrons and

$$D(r) = \frac{1}{2\pi} \int d\Omega_r = \int_0^{\theta_r^{\max}} \sin \theta_r d\theta_r = 1 - \sqrt{1 - \frac{R_\nu^2}{r^2}}. \quad (15)$$

In Equation (14),  $\Delta \equiv m_n - m_p$  is the neutron–proton mass difference,  $m_N = (m_n + m_p)/2$  is the average nucleon mass, the term associated with

$$W_{\nu_e} = \frac{2[1 + 5g_A^2 - 2g_A(1 + f_2)]}{1 + 3g_A^2} \quad (16)$$

is the correction due to weak magnetism and nucleon recoil, and  $G_F$ ,  $V_{ud}$ ,  $g_A$ , and  $f_2$  are the standard constants describing the weak interaction of concern.

### 2.3. Active–Sterile Neutrino Oscillations

We only consider  $\nu_e$ – $\nu_s$  and  $\bar{\nu}_e$ – $\bar{\nu}_s$  oscillations in this paper. We assume that neutrinos emitted with energy  $E$  but from different points on the neutrinosphere have the same flavor evolution as those traveling on the radial trajectory. For a radially propagating  $\nu_e$  emitted with energy  $E$ , the evolution of its wave function

$$\psi_{\nu_e}(E, r) = \begin{pmatrix} a_{\nu_e}(E, r) \\ a_{\nu_s}(E, r) \end{pmatrix} \quad (17)$$

is governed by

$$i \frac{d}{dr} \psi_{\nu_e}(E, r) = \mathbf{H}_{\nu_e}(E, r) \psi_{\nu_e}(E, r), \quad (18)$$

where  $a_{\nu_e}$  ( $a_{\nu_s}$ ) is the amplitude for being a  $\nu_e$  ( $\nu_s$ ), and

$$\mathbf{H}_{\nu_e}(E, r) = \mathbf{H}_{\text{vac}}(E) + \mathbf{H}_{\text{mat}}(r) + \mathbf{H}_{\nu\nu}(r) \quad (19)$$

is the propagation Hamiltonian. The three contributions to this Hamiltonian are

$$\mathbf{H}_{\text{vac}}(E) = \frac{\delta m^2}{4E} \begin{pmatrix} -\cos 2\theta_V & \sin 2\theta_V \\ \sin 2\theta_V & \cos 2\theta_V \end{pmatrix}, \quad (20)$$

where  $\delta m^2$  is the vacuum mass-squared difference and  $\theta_V$  is the vacuum mixing angle,

$$\mathbf{H}_{\text{mat}}(r) = \frac{V_{\text{mat}}(r)}{2} \begin{pmatrix} 1 & 0 \\ 0 & -1 \end{pmatrix}, \quad (21)$$

where

$$V_{\text{mat}}(r) = \frac{\sqrt{2} G_F}{2m_u} \rho(r) [3Y_e(r) - 1] \quad (22)$$

corresponds to neutrino forward scattering on  $e^\pm$ , neutrons, and protons (Wolfenstein 1978; Mikheev & Smirnov 1985; see also, e.g., Sigl & Raffelt 1993), and

$$\mathbf{H}_{\nu\nu}(r) = \frac{V_\nu(r)}{2} \begin{pmatrix} 1 & 0 \\ 0 & -1 \end{pmatrix}, \quad (23)$$

where

$$V_\nu(r) = \frac{\sqrt{2} G_F D(r)^2}{2\pi R_\nu^2} \int \left[ \frac{L_{\nu_e}}{\langle E_{\nu_e} \rangle} f_{\nu_e}(E') P_{\nu_e}(E', r) - \frac{L_{\bar{\nu}_e}}{\langle E_{\bar{\nu}_e} \rangle} f_{\bar{\nu}_e}(E') P_{\bar{\nu}_e}(E', r) \right] dE' \quad (24)$$

corresponds to neutrino forward scattering on other neutrinos (e.g., Fuller et al. 1987; Sigl & Raffelt 1993). In Equation (24),  $P_{\bar{\nu}_e}(E, r)$  is calculated from the amplitude  $a_{\bar{\nu}_e}(E, r)$ , which in turn is determined along with  $a_{\bar{\nu}_s}(E, r)$  by the same flavor evolution equation as Equation (18), except with the Hamiltonian  $\mathbf{H}_{\bar{\nu}_e}(E, r) = \mathbf{H}_{\text{vac}}(E) - \mathbf{H}_{\text{mat}}(r) - \mathbf{H}_{\nu\nu}(r)$ . Because we only consider  $\nu_e$ – $\nu_s$  and  $\bar{\nu}_e$ – $\bar{\nu}_s$  oscillations, there is no flavor evolution for  $\nu_x$  or  $\bar{\nu}_x$ . We further assume that  $\nu_x$  and  $\bar{\nu}_x$  have the same emission characteristics so that their contributions to  $\mathbf{H}_{\nu\nu}(r)$  cancel.

### 2.4. Parameters and Procedures

A number of experiments indicate the existence of a  $\nu_s$  ( $\bar{\nu}_s$ ) that mixes with  $\nu_e$  ( $\bar{\nu}_e$ ) for a range of plausible vacuum mixing

**Table 1**  
Cases of Active–Sterile Neutrino Oscillations

Case	$\delta m^2$ (eV <sup>2</sup> )	$\sin^2 2\theta_\nu$
A	1.75	0.10
B	1.0	0.06
C	0.4	0.04
D	no	oscillations

parameters. As our major goal is to include active–sterile neutrino oscillations in a self-consistent treatment of the wind and to demonstrate their effects, we follow Wu et al. (2014) and consider three sets of  $\delta m^2$  and  $\sin^2 2\theta_\nu$  that are listed in Table 1 and referred to as cases A, B, and C, respectively. For comparison, the case without oscillations is referred to as case D. We plan to survey a broad range of mixing parameters in a separate paper.

To solve the wind equations, we need to specify properties of the PNS, especially the characteristics of its neutrino emission, the inner boundary conditions at the neutrinosphere, and the outer boundary conditions at the CCSN shock. We use the spherical CCSN model of Martínez-Pinedo et al. (2014) as a guide and consider three snapshots at time post-core bounce  $t_{\text{pb}} = 1, 2,$  and  $5$  s, respectively. The PNS mass is taken to be fixed at  $M_{\text{PNS}} = 1.282 M_\odot$ . The neutrinosphere radius  $R_\nu$  for each snapshot is given in Table 2 along with the luminosities and average energies of  $\nu_e, \bar{\nu}_e,$  and  $\nu_x$  at emission. As noted above, the emission characteristics of  $\bar{\nu}_x$  are taken to be identical to those of  $\nu_x$ . We assume that the shock launched by the CCSN explosion is unaffected by active–sterile neutrino oscillations. For the epoch of interest, the region at  $r \gtrsim 10^3$  km enclosed by the shock has approximately the same temperature, which slowly decreases as the shock moves outward. We take the temperature at  $r = 10^3$  km  $\equiv R_b$  as the effective outer boundary condition set up by the CCSN shock. The values of  $T(R_b)$  are given in Table 2 along with the corresponding temperatures  $T(R_\nu)$  at the neutrinosphere. In addition to  $T(R_\nu)$ , the other inner boundary conditions are values of  $\rho(R_\nu)$  and  $Y_e(R_\nu)$ , which are determined by assuming  $\dot{q} = 0$  and  $dY_e/dr = 0$  at the neutrinosphere. Note that for the vacuum mixing parameters of interest,  $\nu_e\text{--}\nu_s$  and  $\bar{\nu}_e\text{--}\bar{\nu}_s$  oscillations can be ignored at the neutrinosphere and  $\rho(R_\nu)$  and  $Y_e(R_\nu)$  correspond to conditions in the absence of neutrino oscillations. Accordingly, we assume that neutrinos and antineutrinos are in their pure active flavor states at the neutrinosphere.

For a specific set of  $\delta m^2$  and  $\sin^2 2\theta_\nu$  and a specific set of boundary conditions, we use the following procedure to determine  $v(r), \rho(r), T(r),$  and  $Y_e(r)$  for the wind: (1) calculate  $\rho(R_\nu)$  and  $Y_e(R_\nu)$  for the corresponding  $T(R_\nu)$  using  $\dot{q}(R_\nu) = 0$  and  $(dY_e/dr)_{R_\nu} = 0$ ; (2) pick an estimated value of  $\dot{M}$  and calculate  $v(R_\nu)$ ; (3) starting from  $r = R_\nu$ , integrate the wind equations along with the equations of  $\nu_e$  and  $\bar{\nu}_e$  flavor evolution up to  $r = R_b$ ; (4) repeat steps 2 and 3 until the value of  $T(R_b)$  given by the wind solution satisfies the outer boundary condition. The corresponding  $\dot{M}$  is the eigenvalue of the mass-loss rate for the wind.

### 3. Results on Neutrino-driven Winds

Below we present the results on the wind for three sets of vacuum mixing parameters (cases A, B, and C in Table 1) and for three snapshots of the CCSN evolution ( $t_{\text{pb}} = 1, 2,$  and  $5$  s).

We also compare these results with those in the absence of neutrino oscillations.

#### 3.1. Mass-loss Rates and Profiles of $v, \rho,$ and $T$

The results on the wind mass-loss rate  $\dot{M}$  for each case of interest are given in Table 3, and those on the profiles of  $v, \rho,$  and  $T$  are shown in Figure 1. For all three snapshots, the wind solutions for the vacuum mixing parameters of case C are very close to those in the absence of neutrino oscillations (case D), whereas the solutions for case A show the largest deviations. The solutions for case B are similar to those for case A for  $t_{\text{pb}} = 1$  s, but become similar to case C for  $t_{\text{pb}} = 5$  s. In addition, the effects of oscillations on  $\dot{M}$  and the profile of  $v$  are much more significant than those on the profiles of  $\rho$  and  $T$ . As case A corresponds to the largest effects of oscillations, we focus on this case in this subsection.

The rate of net energy gain per unit mass  $\dot{q}$  is crucial to the understanding of the wind. This quantity is shown as functions of  $r$  and  $T$ , respectively, in Figures 2(a)–(f). Our inner boundary conditions require  $\dot{q}(R_\nu) = 0$ . Because the rate of cooling is sensitive to  $T$ , it decreases more rapidly than the rate of heating by neutrinos at  $r > R_\nu$ . The resulting net energy gain causes  $\dot{q}$  to increase sharply in the immediate neighborhood of  $r = R_\nu$ . However, the decrease of the neutrino heating rate due to the diminishing neutrino fluxes and any  $\nu_e\text{--}\nu_s$  and  $\bar{\nu}_e\text{--}\bar{\nu}_s$  oscillations takes effect at larger  $r$ . The above two competing factors cause  $\dot{q}$  to peak near the neutrinosphere. At even larger  $r$  corresponding to  $T < 1$  MeV, formation of  $\alpha$ -particles becomes important and the associated energy release results in the other peak of  $\dot{q}$ . At  $T \gtrsim 1$  MeV, neutrino heating by the reactions in Equations 1(a) and 1(b) makes the dominant contribution to  $\dot{q}$ . As the rate of heating by these reactions is substantially reduced by  $\nu_e\text{--}\nu_s$  and  $\bar{\nu}_e\text{--}\bar{\nu}_s$  oscillations in case A, the  $\dot{q}$  in this case is significantly less than that in case D without oscillations. In order to drive the wind, the net energy gain must overcome the gravitational potential of the PNS (Qian & Woosley 1996). So the mass-loss rate of the wind can be estimated as

$$\dot{M} \sim \frac{R_\nu}{GM_{\text{PNS}}} \int_{R_\nu}^{R_b} 4\pi r^2 \rho \dot{q} dr. \quad (25)$$

The reduction of  $\dot{q}$  by oscillations in case A leads to the reduction of  $\dot{M}$  by a factor of  $\approx 2.7, 1.6,$  and  $1.6$  for  $t_{\text{pb}} = 1, 2,$  and  $5$  s, respectively, relative to case D (see Table 3).

Using  $4\pi r^2 \rho \dot{q} = \dot{M} \dot{q}/v$ , we can rewrite Equation (25) as

$$\int_{R_\nu}^{R_b} \frac{\dot{q}}{v} dr \sim \frac{GM_{\text{PNS}}}{R_\nu}. \quad (26)$$

Because the right-hand side of the above equation is fixed for both cases with and without oscillations, the reduction of  $\dot{q}$  by oscillations in case A is expected to be accompanied by the reduction of  $v$  relative to case D (see Figures 1(a)–(c)). With the reduced neutrino heating rate, the wind material in case A must move more slowly so that there is more time for the material to gain the energy required to overcome the gravitational potential of the PNS. We show  $\dot{q}/v$  as a function of  $r$  in Figures 2(g)–(i). It can be seen that except for the region near the neutrinosphere where oscillations give rise to complicated behaviors in case A,  $\dot{q}/v$  is very similar for cases A and D.

Compared to  $v$ , the differences in the profile of  $\rho$  or  $T$  between cases A and D are much smaller (see Figure 1). This

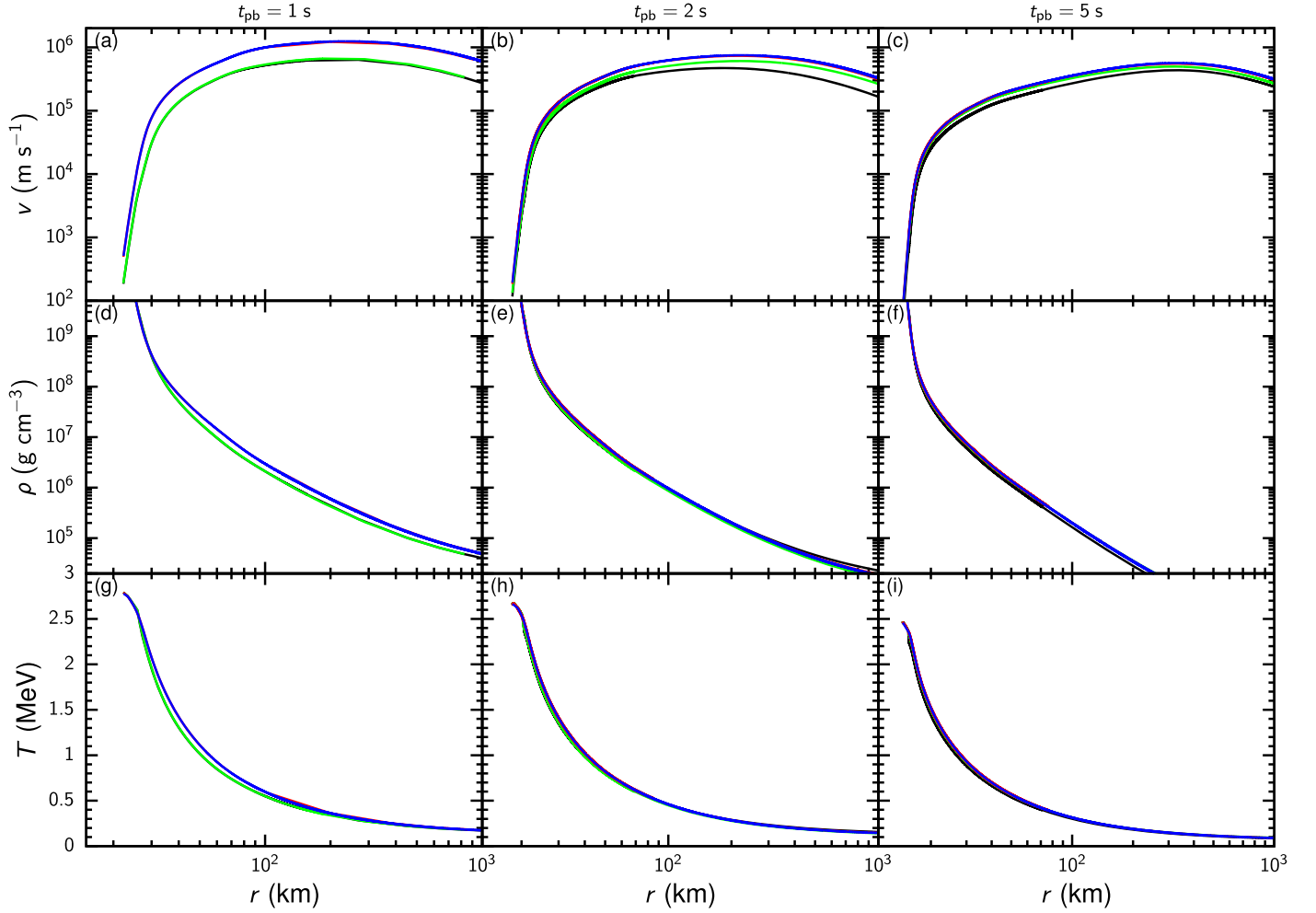


**Figure 1.** Wind profiles of  $v$  (upper row),  $\rho$  (central row), and  $T$  (bottom row) as functions of radius  $r$  at  $t_{\text{pb}} = 1$  s (left column), 2 s (central column), and 5 s (right column) for cases A (black), B (green), C (red), and D (blue). Note that the red and blue curves are indistinguishable.

**Table 2**  
Parameters at the Inner and Outer Boundaries

$t_{\text{pb}}$ (s)	$R_\nu$ (km)	$L_{\nu_e}$	$L_{\nu_\mu}$	$L_{\nu_\tau}$	$\langle E_{\nu_e} \rangle$	$\langle E_{\nu_\mu} \rangle$	$\langle E_{\nu_\tau} \rangle$	$T(R_\nu)$	$T(R_b)$
1	22.25	2.95	3.68	3.83	8.80	12.49	12.34	2.79	0.17
2	18.07	1.67	2.01	2.58	8.43	11.90	11.70	2.68	0.14
5	14.50	0.82	0.83	1.42	7.79	10.17	10.47	2.47	0.09

**Note.** Neutrino luminosities are given in units of  $10^{51}$  erg  $\text{s}^{-1}$ . Average neutrino energies and temperatures are given in units of MeV.

**Table 3**  
Mass-loss Rates in Units of  $M_\odot \text{s}^{-1}$

$t_{\text{pb}}$ (s)	A	B	C	D
1	6.95(-5)	7.10(-5)	1.86(-4)	1.87(-4)
2	2.40(-5)	2.76(-5)	3.80(-5)	3.81(-5)
5	2.82(-6)	4.16(-6)	4.50(-6)	4.51(-6)

**Note.** The letters refer to the sets of vacuum mixing parameters in Table 1 and  $X(Y)$  denotes  $X \times 10^Y$ .

result is expected for  $T$  because  $T(R_\nu)$  and  $T(R_b)$  are fixed at the inner and outer boundaries for all cases. Indeed, Figure 3 shows that relative to case D, the reduction in the neutrino heating rate by oscillations in case A causes a decrease in  $T$  by at most  $\sim 6\%$ ,  $3\%$ , and  $4\%$  for  $t_{\text{pb}} = 1, 2,$  and  $5$  s, respectively. This

initial decrease is compensated as the slower wind material in case A gains energy at the reduced neutrino heating rate over a longer time than case D so that the same  $T(R_b)$  is obtained. The similar profiles of  $T$  and  $\dot{q}/v$  for cases A and D result in similar profiles of  $\dot{q}/(vT)$  (see Figures 2(j)–(l)). Because the total entropy per baryon  $S_{\text{tot}}$  as a function of  $r$  can be estimated as

$$S_{\text{tot}}(r) \sim S_{\text{tot}}(R_\nu) + \int_{R_\nu}^r \frac{m_u \dot{q}}{Tv} dr, \quad (27)$$

similar profiles of  $\dot{q}/(vT)$  lead to similar profiles of  $S_{\text{tot}}$  for cases A and D. As shown in Figure 4, relative to case D, the largest deviation of  $S_{\text{tot}}$  for case A is an increase by  $\sim 16\%$ ,  $5\%$ , and  $5\%$  for  $t_{\text{pb}} = 1, 2,$  and  $5$  s, respectively. Because  $S_{\text{tot}}(r)$  mainly depends on  $T$  and  $\rho$ , being approximately  $\propto T^3/\rho$  (Qian & Woosley 1996), similar profiles of  $S_{\text{tot}}$  and  $T$  mean similar

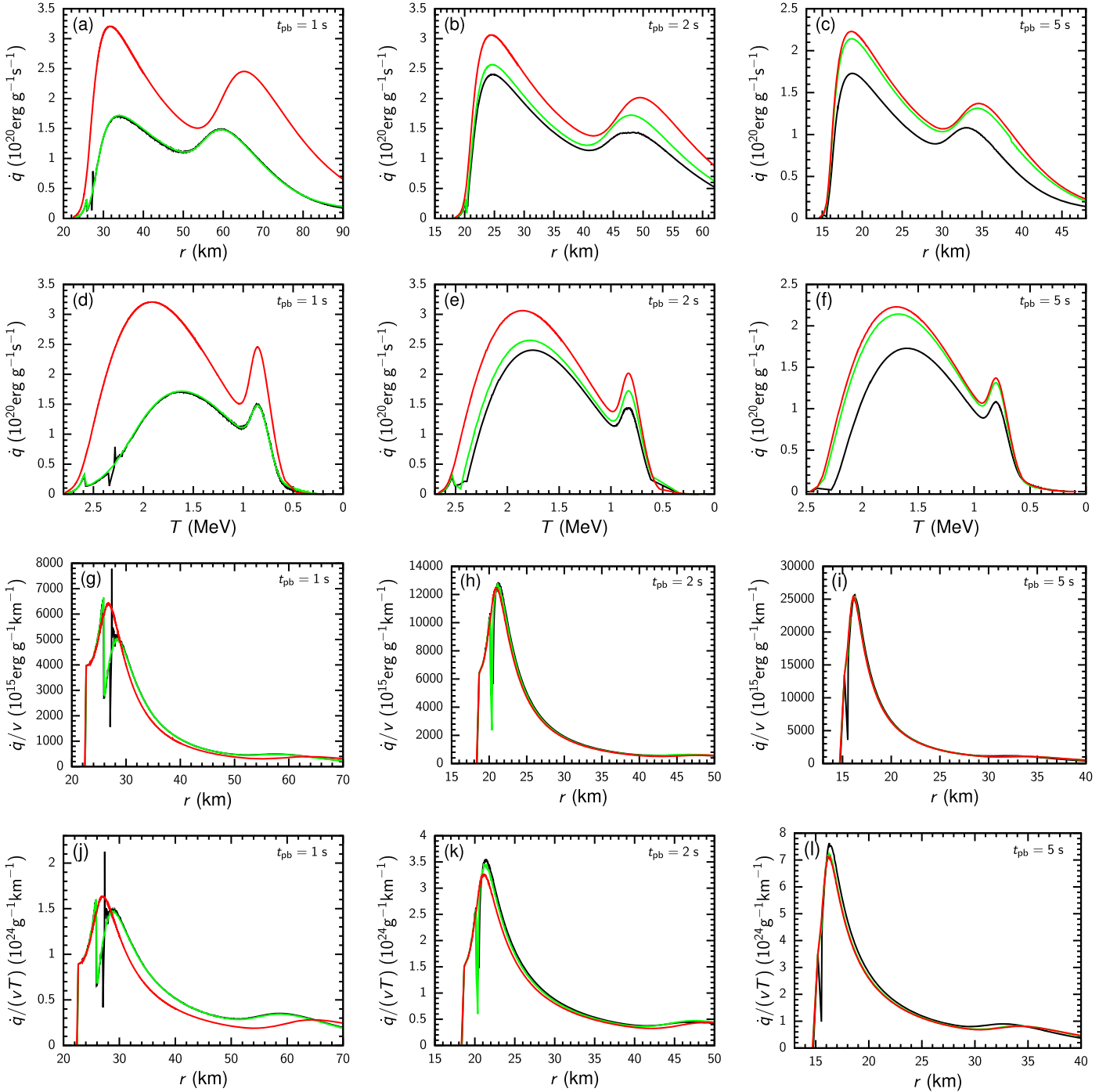


**Figure 2.** Net heating rates  $\dot{q}$  as functions of radius  $r$  (upper row) and temperature  $T$  (second row), as well as  $\dot{q}/v$  (third row) and  $\dot{q}/(vT)$  (bottom row) as functions of  $r$  at  $t_{pb} = 1$  s (left column), 2 s (central column), and 5 s (right column) for cases A (black), B (green), and C (red).

profiles of  $\rho$  as well. As  $\dot{M} = 4\pi r^2 \rho v$ , the reduction of  $\dot{M}$  by oscillations in case A mostly translates into the reduction of  $v$  relative to case D, which is in agreement with the discussion in the preceding two paragraphs.

### 3.2. Active–Sterile Neutrino Oscillations and Effects on the $Y_e$ Profile

In addition to the effects on the mass-loss rates and profiles of  $v$ ,  $\rho$ , and  $T$  discussed above, active–sterile neutrino oscillations can change the evolution of  $Y_e$ , which is critical

to nucleosynthesis. Further, the intricate feedback between the evolution of  $Y_e$  and survival probabilities of  $\nu_e$  and  $\bar{\nu}_e$  leads to a range of interesting behaviors of active–sterile neutrino oscillations, which are presented below. For convenience, we denote the cases under discussion by the letter for the vacuum mixing parameters (see Table 1) followed by the numerical value of the  $t_{pb}$  for the snapshot (see Table 2). For example, case A1 refers to  $\delta m^2 = 1.75 \text{ eV}^2$ ,  $\sin^2 2\theta_V = 0.10$ , and  $t_{pb} = 1$  s.

In Figures 5(a)–(c) we show the  $Y_e$  profiles for all the cases. Because  $\nu_e$  absorption on neutrons increases whereas  $\bar{\nu}_e$

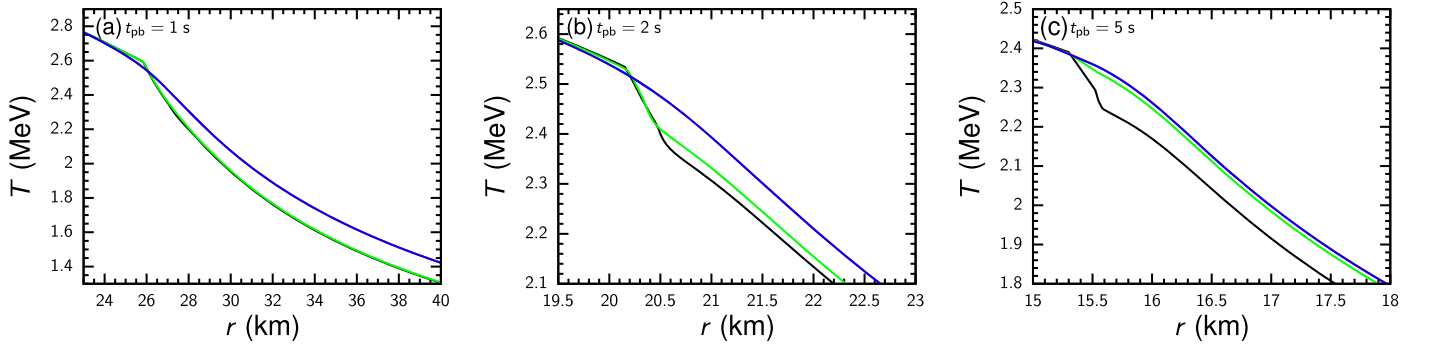


**Figure 3.** Wind temperature  $T$  near the onset of active–sterile neutrino oscillations as a function of radius  $r$  at  $t_{pb} = 1$  s (a), 2 s (b), and 5 s (c) for cases A (black), B (green), C (red), and D (blue). Note that the red and blue curves are indistinguishable.

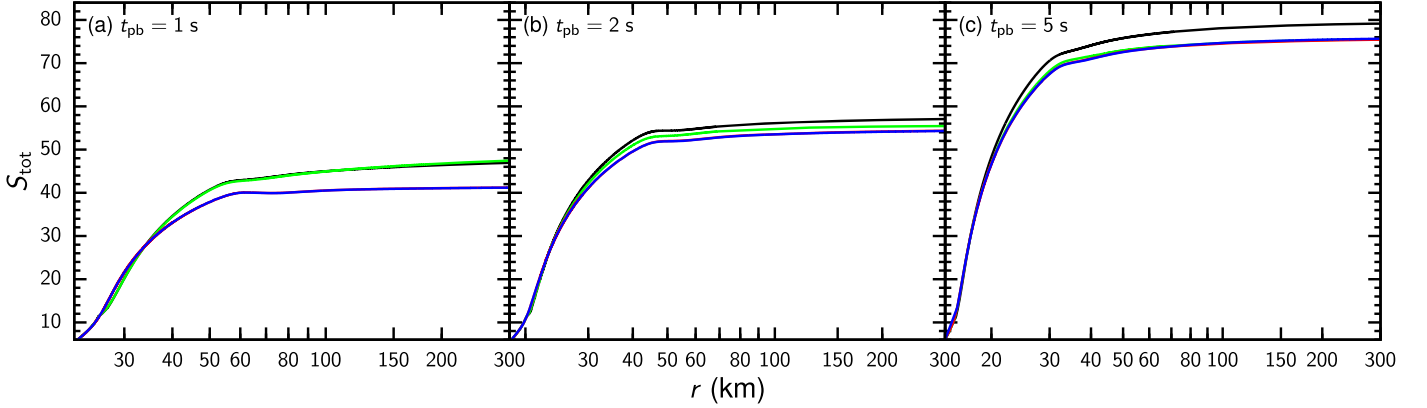


**Figure 4.** Total entropy  $S_{tot}$  as a function of radius  $r$  at  $t_{pb} = 1$  s (a), 2 s (b), and 5 s (c) for cases A (black), B (green), C (red), and D (blue). Note that the red and blue curves are indistinguishable.

absorption on protons decreases  $Y_e$ , the change of  $Y_e$  due to active–sterile neutrino oscillations approximately follows the corresponding change of the ratio  $\lambda_{\nu_e n}/\lambda_{\bar{\nu}_e p}$  for the rates of these reactions. This ratio is shown as a function of  $r$  in Figures 5(d)–(f) for all the cases. Compared with the corresponding cases of no oscillations, cases C1, C2, and C5 show essentially no change of  $\lambda_{\nu_e n}/\lambda_{\bar{\nu}_e p}$ , and hence  $Y_e$ , up to  $r \sim 90$ , 60, and 40 km, respectively. Although  $\lambda_{\nu_e n}/\lambda_{\bar{\nu}_e p}$  changes greatly at larger radii for these three cases, there are no corresponding changes of  $Y_e$  because  $Y_e$  has essentially frozen out at such large radii due to the small rates of the pertinent reactions. Therefore, active–sterile neutrino oscillations have negligible effects on the  $Y_e$  profiles in cases C1, C2, and C5. In contrast, there are significant changes of the  $Y_e$  profiles due to oscillations in all the other cases. With the exception of case A5, active–sterile neutrino oscillations in these cases reduce  $\lambda_{\nu_e n}/\lambda_{\bar{\nu}_e p}$ , and hence  $Y_e$ , relative to the corresponding cases of no oscillations. Case A5 is unique in that oscillations increase  $\lambda_{\nu_e n}/\lambda_{\bar{\nu}_e p}$ , and hence  $Y_e$ . Note again that  $Y_e$  eventually freezes out and does not track the effects of oscillations on  $\lambda_{\nu_e n}/\lambda_{\bar{\nu}_e p}$  at large radii.

To understand the effects of active–sterile neutrino oscillations on  $\lambda_{\nu_e n}$  and  $\lambda_{\bar{\nu}_e p}$ , we show in Figure 6 the average survival probabilities  $\langle P_{\nu_e}(r) \rangle$  and  $\langle P_{\bar{\nu}_e}(r) \rangle$  of  $\nu_e$  and  $\bar{\nu}_e$ , respectively, as functions of  $r$  for all the relevant cases. Here, for example,

$$\langle P_{\nu_e}(r) \rangle = \int P_{\nu_e}(E, r) f_{\nu_e}(E) dE, \quad (28)$$

where  $f_{\nu_e}(E)$  is the normalized  $\nu_e$  spectrum at emission (see Equation (6)). The flavor evolution of  $\nu_e$  and  $\bar{\nu}_e$  is sensitive to

the Mikheyev–Smirnov–Wolfenstein-like (MSW-like) resonances (Wolfenstein 1978; Mikheev & Smirnov 1985) corresponding to

$$V_{tot}(r) = V_{mat}(r) + V_\nu(r) = \pm \frac{\delta m^2}{2E} \cos 2\theta_V, \quad (29)$$

where the plus and minus signs are for  $\nu_e$ – $\nu_s$  and  $\bar{\nu}_e$ – $\bar{\nu}_s$  oscillations, respectively. In the above equation,  $V_{tot}$  is the total effective potential for flavor evolution with contributions  $V_{mat}$  (Equation (22)) and  $V_\nu$  (Equation (24)) from neutrino forward scattering on matter particles and other neutrinos, respectively. As a first approximation, the radii for the resonances can be estimated from

$$V_{mat}(r) = \frac{\sqrt{2} G_F}{2m_u} \rho(r) [3Y_e(r) - 1] \sim \pm \frac{\delta m^2}{2E} \cos 2\theta_V. \quad (30)$$

The term  $\rho(3Y_e - 1)$  in  $V_{mat}$  gives rise to two types of resonances. The inner resonances occur for both  $\nu_e$ – $\nu_s$  and  $\bar{\nu}_e$ – $\bar{\nu}_s$  oscillations close to the neutrinosphere as  $Y_e$  increases from below to slightly above  $1/3$ . Here  $G_F \rho/m_u$  far exceeds  $\delta m^2/E$  and the resonance conditions are met in the region with  $Y_e \sim 1/3$ . In contrast, the outer resonances occur only for  $\nu_e$ – $\nu_s$  oscillations at much larger radii. Here  $Y_e$  is significantly above  $1/3$  and the resonance condition is met only for the upper sign in Equation (30) due to the much smaller  $\rho$ .

The main features of oscillations in cases C1, C2, and C5 are the two types of resonances outlined above. Using  $V_{tot}$  instead of  $V_{mat}$  in the resonance conditions does not change the

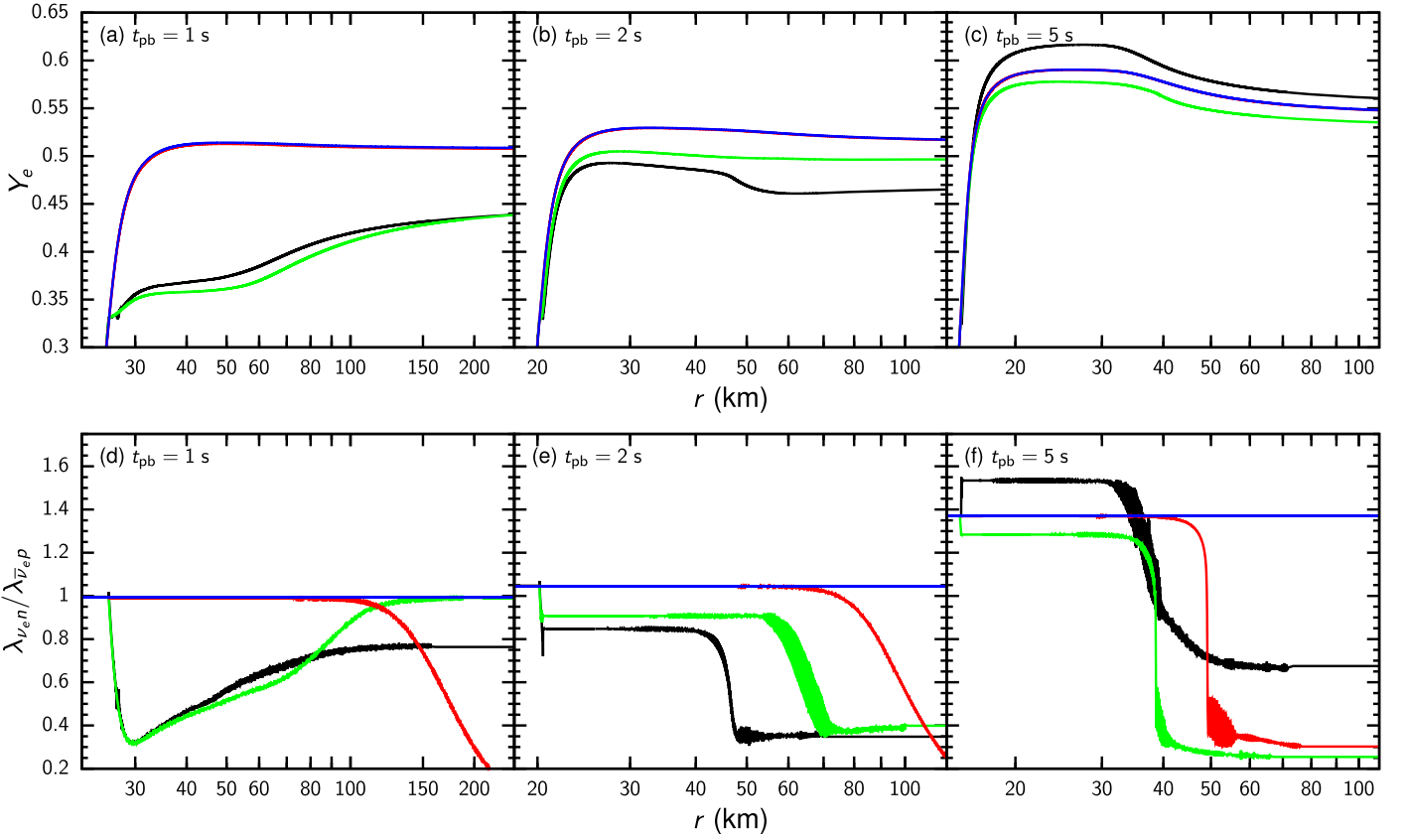


**Figure 5.** Electron fraction  $Y_e$  (upper row) and ratio of the rates  $\lambda_{\nu_e n} / \lambda_{\bar{\nu}_e p}$  (bottom row) as functions of radius  $r$  at  $t_{pb} = 1$  s (left column), 2 s (central column), and 5 s (right column) for cases A (black), B (green), C (red), and D (blue). Note that the red and blue curves for  $Y_e$  are indistinguishable.

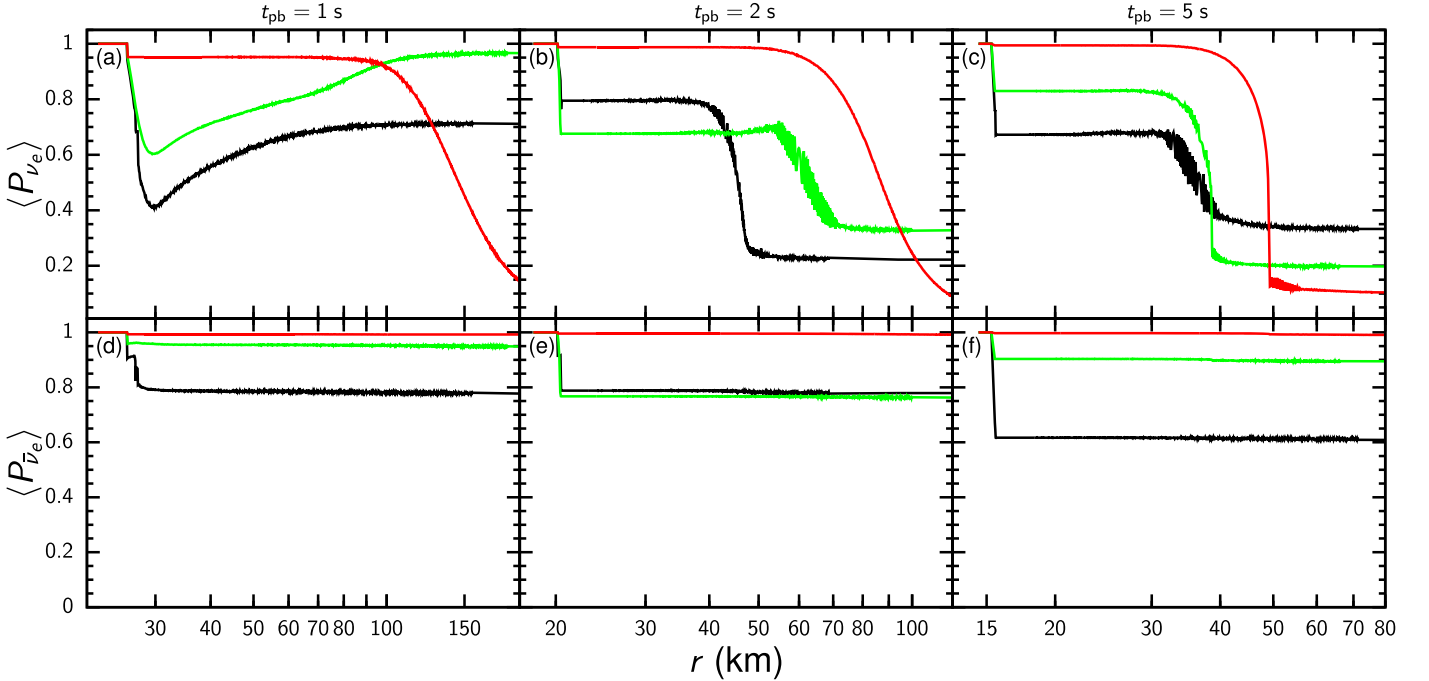


**Figure 6.** Average survival probabilities for  $\nu_e$  and  $\bar{\nu}_e$  as functions of radius at  $t_{pb} = 1$  s (left column), 2 s (central column), and 5 s (right column) for cases A (black), B (green), and C (red).

discussion qualitatively except for the outer resonance in case C5. As shown in Figure 7, for a fixed  $\nu_e$  or  $\bar{\nu}_e$  energy, the inner resonance condition is met at a slightly smaller  $r$  when  $V_{\text{tot}}$  is used. With the small values of the corresponding  $\delta m^2$  and

$\sin^2 2\theta_V$ , flavor evolution through the inner resonances is rather nonadiabatic for  $\nu_e$  and  $\bar{\nu}_e$  of typical energies, which leads to large  $\langle P_{\nu_e}(r) \rangle$  and  $\langle P_{\bar{\nu}_e}(r) \rangle$  immediately following the inner resonances in cases C1, C2, and C5 (see Figure 6). Using  $V_{\text{tot}}$



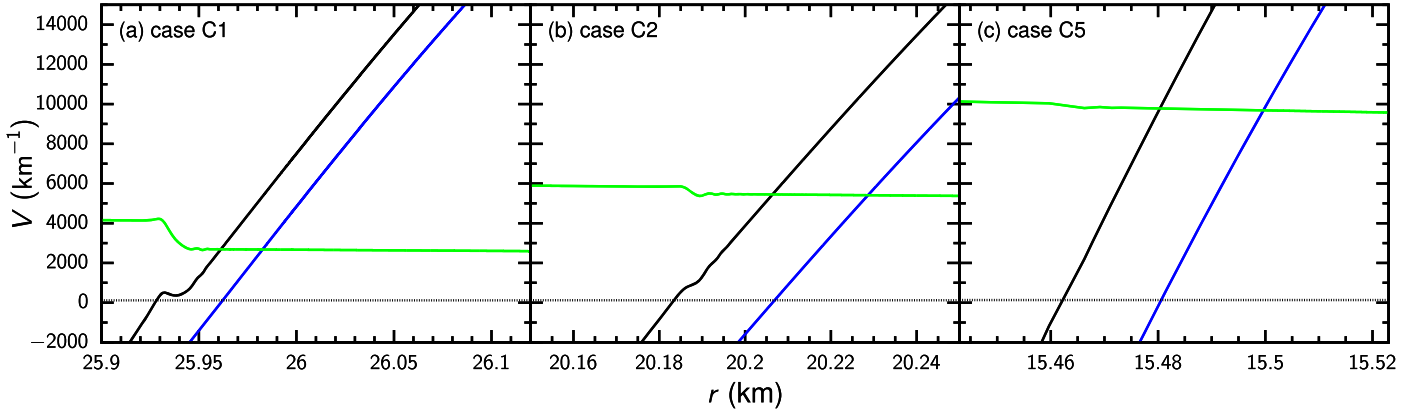


**Figure 7.** Effective potentials  $V_{\text{tot}}$  (solid black),  $V_{\text{mat}}$  (solid blue), and  $V_{\nu}$  (solid green) as functions of radius  $r$  near the inner resonances at  $t_{\text{pb}} = 1$  s (a), 2 s (b), and 5 s (c) for case C. For comparison, dotted black lines correspond to  $\delta m^2 / (2 \langle E_{\nu_e} \rangle)$ .

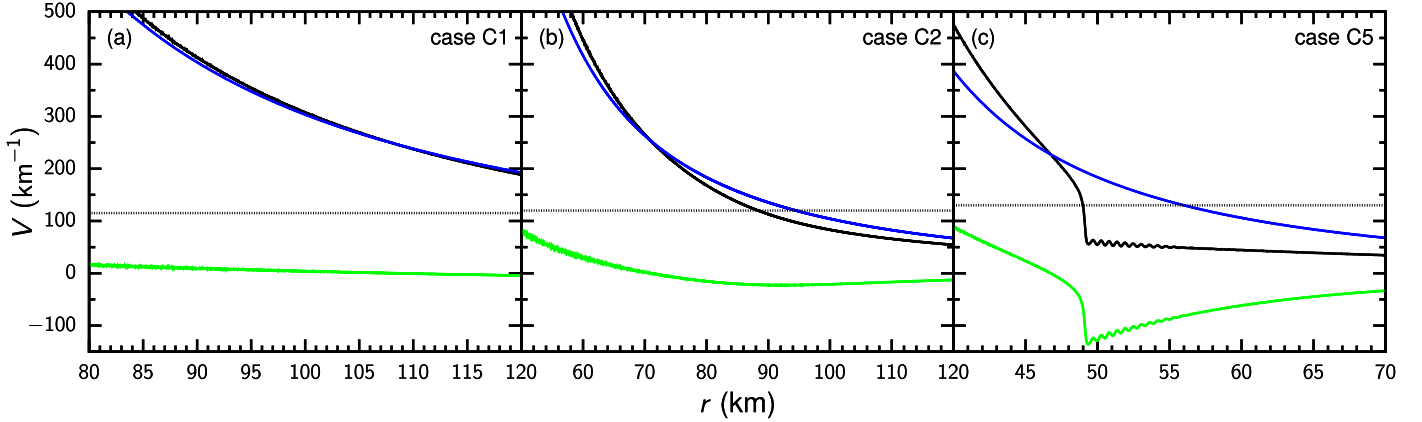


**Figure 8.** Effective potentials  $V_{\text{tot}}$  (solid black),  $V_{\text{mat}}$  (solid blue), and  $V_{\nu}$  (solid green) as functions of radius  $r$  near the outer resonances at  $t_{\text{pb}} = 1$  s (a), 2 s (b), and 5 s (c) for case C. For comparison, dotted black lines correspond to  $\delta m^2 / (2 \langle E_{\nu_e} \rangle)$ .

again changes only slightly the radius of the outer resonance for a specific  $\nu_e$  energy in cases C1 and C2 (see Figures 8(a)–(b)). Because  $V_{\text{tot}}$  changes much more slowly at large radii,  $\nu_e$  flavor evolution through the outer resonances is rather adiabatic, which results in a large decrease of  $\langle P_{\nu_e}(r) \rangle$  following the outer resonances in cases C1 and C2 (see Figures 6(a)–(b)). The outer resonance in case C5 becomes qualitatively different when  $V_{\text{tot}}$  is used. Here the magnitude of  $V_{\nu}$  becomes comparable to that of  $V_{\text{mat}}$ , and  $V_{\text{tot}}$  essentially becomes flat (see Figure 8(c)). This behavior resembles that of the matter-neutrino resonances for active–active neutrino oscillations (e.g., Malkus et al. 2016; Wu et al. 2016a), and results in efficient conversion of  $\nu_e$  with typical energies in case C5 (see Figure 6(c)). However, because the outer resonances occur after the freeze-out of  $Y_e$ , they have little impact on the  $Y_e$  profiles. Therefore, active–sterile neutrino oscillations in cases C1, C2, and C5 only have small effects on all the wind properties, and will not be discussed any further.

As can be seen clearly in Figures 6(b)–(c), the outer resonances also occur to further decrease  $\langle P_{\nu_e}(r) \rangle$  in cases A2, B2, A5, and B5. For case B2, the outer resonances are similar to those in case C2. For cases A2, A5, and B5,  $V_{\nu}$  becomes significant and the behavior of the outer resonances starts to approach that in case C5. However, all outer resonances occur at large radii corresponding to small rates of the pertinent neutrino reactions. Consequently, their effects on the  $Y_e$  profiles and other wind properties are very limited. Below we focus on the inner resonances, which dominate the overall flavor

evolution in cases A1 and B1 as well as produce in general the predominant effects of active–sterile neutrino oscillations on all the wind properties including the  $Y_e$  profiles.

A full understanding of the inner resonances for  $\nu_e$ – $\nu_s$  and  $\bar{\nu}_e$ – $\bar{\nu}_s$  oscillations requires a careful examination of how the conditions in Equation (29) are fulfilled by the contributions  $V_{\text{mat}}$  and  $V_{\nu}$  to  $V_{\text{tot}}$ . These quantities are shown as functions of  $r$  for cases A1, B1, A2, B2, A5, and B5 in Figure 9. All these cases have significant plateaus of  $V_{\text{tot}} \sim \pm \delta m^2 \cos 2\theta_V / (2E)$  corresponding to inner resonances for  $\nu_e$  and  $\bar{\nu}_e$  of typical energies. These plateaus can be divided into three categories: (1) a stable plateau spanning  $>1$  km as in case B1; (2) an unstable one spanning  $\sim 0.1$ – $0.3$  km as in cases A2, B2, A5, and B5; and (3) a wide one interrupted by an instability as in case A1. For all three categories, the plateau results from the near cancellation of  $V_{\text{mat}}$  and  $V_{\nu}$ , each of which has a magnitude far exceeding that of  $V_{\text{tot}}$  for the most part of the corresponding region. The  $Y_e$  in this region is nearly constant and stays close to one-third. This dramatic flattening of the  $Y_e$  profile corresponding to the inner resonances is shown for case A2 as an example in Figure 10.

Formation of the plateau of  $V_{\text{tot}}$  merits a detailed follow-up study. Here we only offer a qualitative sketch of the possible underlying mechanism as illustrated in Figure 11. The total potential  $V_{\text{tot}}$  and the vacuum mixing parameters  $\delta m^2$  and  $\sin^2 2\theta_V$  control the flavor evolution of  $\nu_e$  and  $\bar{\nu}_e$ , mostly through the occurrence of resonances. This evolution determines the survival probabilities  $P_{\nu_e}$  and  $P_{\bar{\nu}_e}$ , which immediately

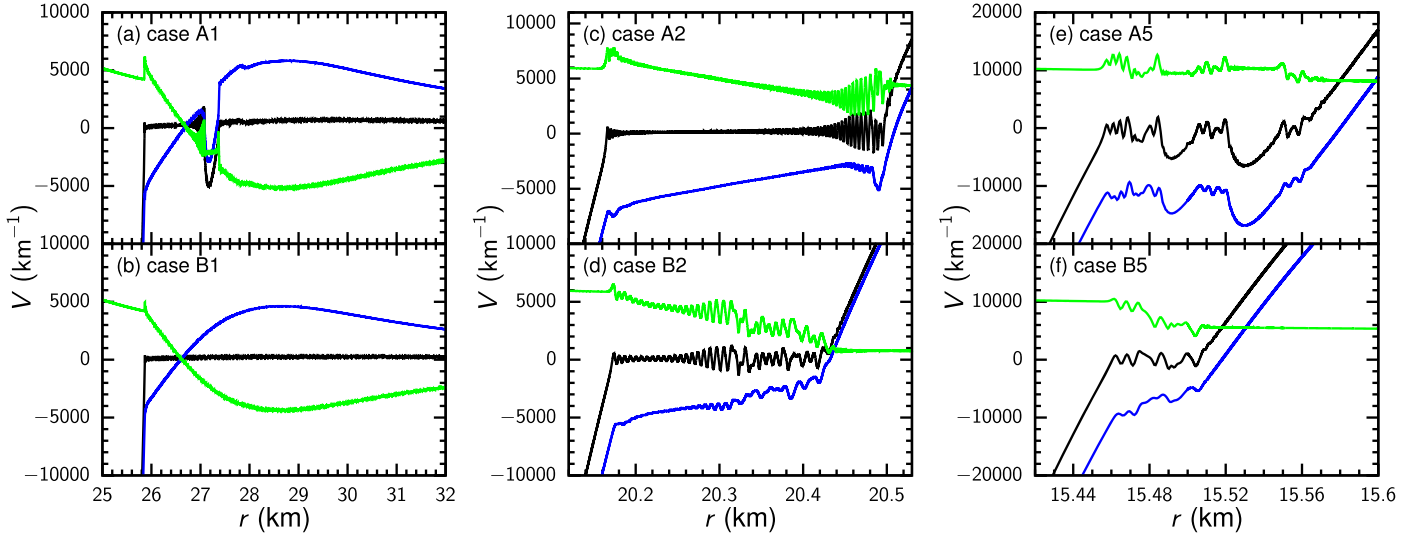


**Figure 9.** Effective potentials  $V_{\text{tot}}$  (black),  $V_{\text{mat}}$  (blue), and  $V_\nu$  (green) as functions of radius  $r$  near the inner resonances at  $t_{\text{pb}} = 1$  s (left column), 2 s (central column), and 5 s (right column) for cases A (top row) and B (bottom row).

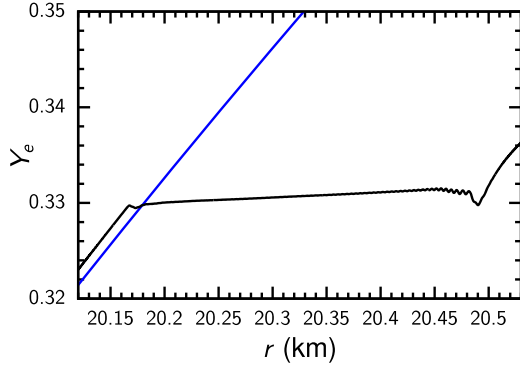


**Figure 10.** Profiles of electron fraction  $Y_e$  as functions of radius  $r$  near the inner resonances at  $t_{\text{pb}} = 2$  s for cases A (black) and D (blue).

modify the contribution  $V_\nu$  from neutrino forward scattering on other neutrinos to  $V_{\text{tot}}$ . The above factors form the first feedback loop of flavor evolution. In addition,  $P_{\nu_e}$  and  $P_{\bar{\nu}_e}$  directly modify the rates  $\lambda_{\nu_e n}$  and  $\lambda_{\bar{\nu}_e p}$ , which control the evolution of  $Y_e$ . In turn,  $Y_e$  determines the contribution  $V_{\text{mat}}$  from neutrino forward scattering on matter particles to  $V_{\text{tot}}$ . These factors form the second feedback loop of flavor evolution. Clearly, the first loop would not operate were  $V_\nu$  far smaller than  $V_{\text{mat}}$  in magnitude, and the second loop would not operate if  $\lambda_{\nu_e n}$  and  $\lambda_{\bar{\nu}_e p}$  were too small to change  $Y_e$  significantly. Consequently, both loops become ineffective at sufficiently large radii, where  $V_\nu$ ,  $\lambda_{\nu_e n}$ , and  $\lambda_{\bar{\nu}_e p}$  are too small due to the geometric dilution of neutrino fluxes. In contrast, both loops are expected to be efficient close to the neutrinosphere, thereby forming the plateau of  $V_{\text{tot}}$  for the inner resonances. However, instabilities appear to develop in the feedback loops under some conditions. Whether and how these instabilities can develop under different conditions might explain the three categories of plateaus presented above. We plan to investigate the feedback loops and associated instabilities in the follow-up study. We also note that those outer resonances similar to the matter-neutrino resonances (e.g., as shown in Figure 8(c) for case C5) are governed by only the first feedback loop described above.

#### 4. Results on Nucleosynthesis

In this section, we discuss the impact of active–sterile neutrino oscillations on the production of heavy elements in neutrino-driven winds. From our wind models, we take a specific set of  $v$ ,  $\rho$ , and  $T$  profiles and use  $dt = dr/v$  to define the evolution of  $\rho(t)$  and  $T(t)$  for a mass element as it moves through the wind. We use the same established nuclear reaction network as in Wu et al. (2016b) to calculate the evolution of the number fraction, or abundance, of each nucleus. We start the network calculation at an initial temperature of  $T = 20$  GK, for which the nuclear composition is dominated by free nucleons. We take the detailed nuclear abundances from the NSE involving all the nuclei in the network for  $20 \geq T \geq 10$  GK when NSE holds very well, and evolve the nuclear abundances with the full reaction network for  $T < 10$  GK. Throughout the nucleosynthesis calculations, we follow the evolution of  $Y_e$  using the rates of  $\nu_e$  and  $\bar{\nu}_e$  absorption and  $e^\pm$  capture on free nucleons as calculated by the wind models. The resulting evolution of  $Y_e(t)$  is in excellent agreement with that calculated directly from the wind models, which always assume a simple NSE composition with free nucleons and  $\alpha$ -particles only. We have also checked that  $\dot{q}_\alpha$ , the rate of energy gain per unit mass from  $\alpha$ -particle formation used in the wind models, is a good approximation based on the evolution of nuclear abundances in the network calculations. Therefore, the simple nuclear composition assumed in the wind models is sufficiently accurate for modeling the wind dynamics and the evolution of  $Y_e$ .

For the evolution of  $\rho(t)$  and  $T(t)$  covered by all our wind models, the  $Y_e$  values at  $T \lesssim 5$  GK are critical to the nucleosynthesis. A more convenient parameter is the corresponding neutron excess  $\delta = 1 - 2Y_e$ . For  $Y_e \sim 0.5$  with  $|\delta| \lesssim 0.02$ , mainly the Fe group nuclei (mass numbers of  $A \sim 56$  and atomic numbers of  $Z \sim 28$ ) are produced. For  $Y_e > 0.5$  with  $\delta < -0.02$ , the wind is sufficiently proton-rich and the nuclear flow proceeds beyond the Fe group nuclei through the  $\nu p$ -process (Frohlich et al. 2006). During this process,  $\bar{\nu}_e$  absorption on protons can maintain a significant neutron abundance to facilitate  $(n, p)$  reactions after reactions between charged particles freeze out. In contrast, for  $Y_e < 0.5$  with

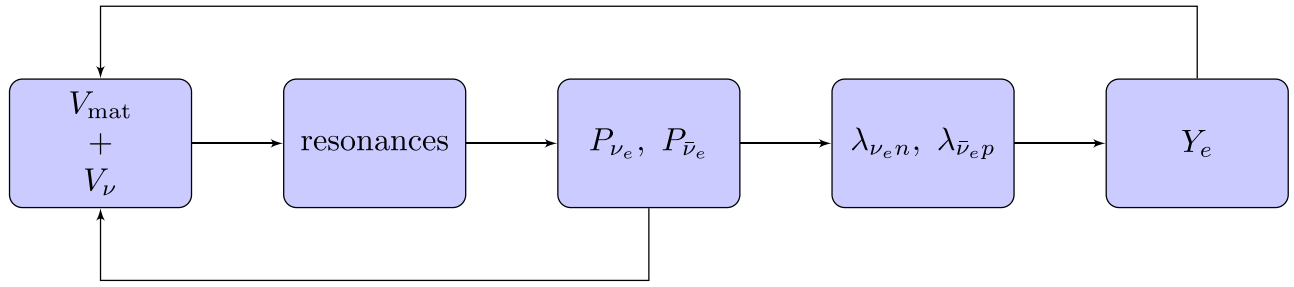


Figure 11. Sketch of the feedback loops for active-sterile neutrino oscillations in the wind. See the text for details.

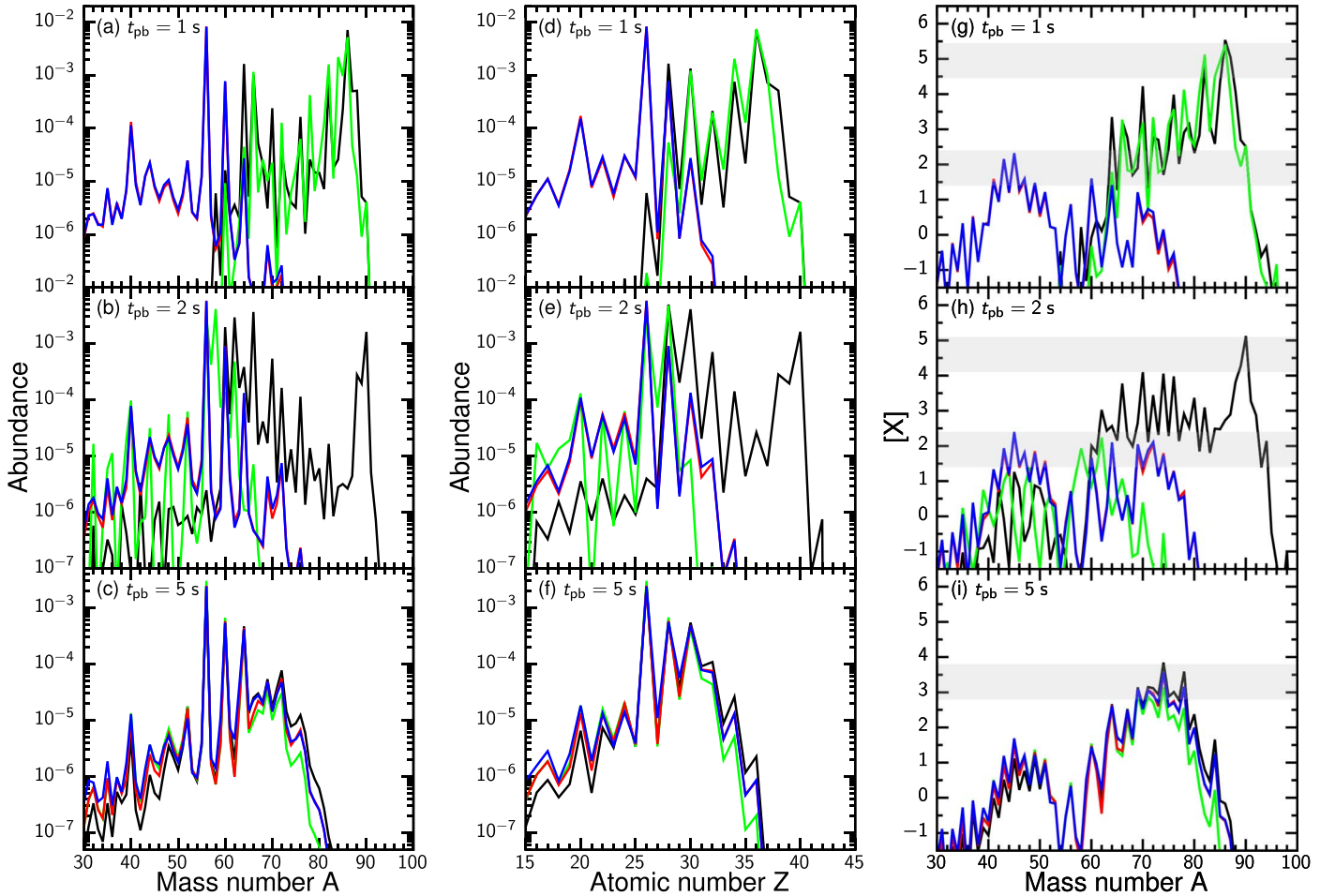
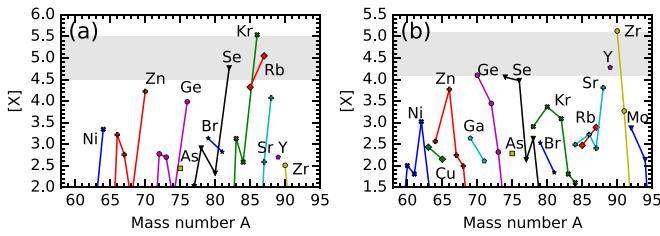


Figure 12. Abundances as functions of mass number (left column) and atomic number (central column), as well as logarithmic production factors as functions of mass number (right column) at  $t_{\text{pb}} = 1$  s (upper row), 2 s (central row), and 5 s (bottom row) for cases A (black), B (green), C (red), and D (blue). The effective production band is indicated by the gray region in the right column. Note that the red and blue curves are almost indistinguishable.

$\delta > 0.02$ , the wind is sufficiently neutron-rich and the nuclear flow proceeds beyond the Fe group nuclei much more efficiently through the  $\alpha$ -process (Woosley & Hoffman 1992).

Figure 12 shows the final abundances produced in all our wind models as functions of mass number  $A$  (left panels) and atomic number  $Z$  (middle panels), respectively. In the absence of neutrino oscillations, the wind is generally proton-rich and becomes more so for the later epochs of the CCSN evolution, with typical values of  $Y_e \sim 0.51, 0.52,$  and  $0.55$  for cases D1, D2, and D5, respectively (see Figure 5). Consequently, nucleosynthesis shifts from dominant production of Fe group nuclei for case D1 to increasing production of heavier nuclei

through the  $\nu p$ -process for cases D2 and D5. This trend is more clearly shown in the right panels of Figure 12 in terms of the logarithmic production factor  $[X] = \log(X/X_\odot)$ , where  $X$  is the mass fraction of a nucleus produced in the wind and  $X_\odot$  is the corresponding value in the solar system. For understanding how the solar composition is obtained by mixing the nucleosynthesis contributions from various astrophysical sources, values of  $[X]$  are more important than the abundances produced by a source. For example,  $^{45}\text{Sc}$  has the highest value of  $[X] \approx 2.3$  among all the nuclei produced by the wind in case D1, while  $^{56}\text{Fe}$  has the highest abundance but a much smaller value of  $[X] \approx 0.9$ . This result means that even if all the  $^{45}\text{Sc}$  in the



**Figure 13.** Production factors as functions of mass number for case A at  $t_{\text{pb}} = 1$  s (a) and 2 s (b). Isotopes of the same element are connected by line segments. The effective production band is indicated by the gray region.

solar system came from sources like this wind, these sources could have contributed only  $\approx 4\%$  of the solar  $^{56}\text{Fe}$ . The horizontal bands in Figures 12–13 indicate  $[X]$  within 1 dex of the highest value. Nuclei within these bands would be the most relevant for contributions to the solar composition.

Because active–sterile neutrino oscillations have little impact on the  $Y_e$  profiles in cases C1, C2, and C5, nucleosynthesis in these cases is essentially identical to that in the corresponding cases of no oscillations. In addition, all cases have similar nucleosynthesis for  $t_{\text{pb}} = 5$  s because the corresponding winds are similarly proton-rich (see Figure 12). In contrast, oscillations greatly reduce the  $Y_e$  values in cases A1, B1, and A2 (see Figure 5), and dramatically alter the nucleosynthesis to produce nuclei far beyond the Fe group (see Figure 12). The largest  $[X]$  is  $\approx 5.5$  and  $5.4$  for  $^{86}\text{Kr}$  in cases A1 and B1, respectively, and is  $\approx 5.1$  for  $^{90}\text{Zr}$  in case A2 (see Figure 13). Both nuclei have a magic number (50) of neutrons and are produced by the  $\alpha$ -process. Finally, oscillations also reduce  $Y_e$  significantly in case B2, but the resulting values of  $Y_e \sim 0.5$  correspond to a very small  $|\delta|$ . Consequently, case B2 has the least extensive production of nuclei beyond the Fe group among all the cases for  $t_{\text{pb}} = 2$  s. Specifically,  $^{62}\text{Ni}$  and  $^{58}\text{Ni}$  have the two largest  $[X]$  values of  $\approx 2.2$  and  $1.9$ , respectively, in this case, while  $^{45}\text{Sc}$  and  $^{72}\text{Ge}$  have the two largest  $[X]$  values of  $\approx 2.4$  and  $2.1$ , respectively, in case D2.

## 5. Conclusions

We have included active–sterile neutrino oscillations in a steady-state model of the neutrino-driven wind and self-consistently treated the effects of oscillations on the  $\nu$ ,  $\rho$ ,  $T$ , and  $Y_e$  profiles of the wind. Compared to previous studies (e.g., Nunokawa et al. 1997; McLaughlin et al. 1999; Tamborra et al. 2012; Wu et al. 2014; Pllumbi et al. 2015) that addressed only the effects on the  $Y_e$  profile, our study represents a significant step forward. Among the three sets of vacuum mixing parameters adopted here (see Table 1), we find that only those of case C with  $\delta m^2 = 0.4$  eV<sup>2</sup> produce negligible effects on the wind. In contrast, those of cases A and B with  $\delta m^2 = 1.75$  and  $1.0$  eV<sup>2</sup>, respectively, significantly change the wind dynamics in addition to the  $Y_e$  profile. Specifically, the mass-loss rate is reduced by a factor of  $\approx 2.7$ ,  $1.6$ , and  $1.6$  for  $t_{\text{pb}} = 1$ ,  $2$ , and  $5$  s in cases A1, A2, and A5, respectively (see Table 3). This reduction translates into a similar reduction of the wind velocity and is caused by the reduced heating as  $\nu_e$  and  $\bar{\nu}_e$  are converted into their sterile counterparts. While the effects of oscillations on the  $\rho$  and  $T$  profiles are much smaller, the resulting increases in  $S_{\text{tot}}$  by  $\sim 15\%$ ,  $5\%$ , and  $5\%$  in cases A1, A2, and A5, respectively (see Figure 4), are still noticeable.

With respect to nucleosynthesis, the most important effects of active–sterile neutrino oscillations are the resulting changes of  $Y_e$ , which range from significant in cases B2, A5, and B5 to large in cases A1, B1, and A2 (see Figure 5). With the large reduction of  $Y_e$  in the latter three cases, nucleosynthesis is dramatically altered (see Figures 12–13). For cases D1 and D2 with no oscillations, the final abundance pattern is characterized by the largest  $[X] \approx 2.3$  and  $2.4$ , respectively, for  $^{45}\text{Sc}$ . In contrast,  $^{86}\text{Kr}$  is produced with the largest  $[X] \approx 5.5$  and  $5.4$  in cases A1 and B1, respectively, and  $^{90}\text{Zr}$  is produced with the largest  $[X] \approx 5.1$  in case A2. Not only do oscillations change the dominant nuclei produced in these cases, but they also greatly amplify the potential contributions from the corresponding winds to the solar composition. The effects of oscillations are also large but less dramatic in case B2, where  $^{62}\text{Ni}$  is produced with the largest  $[X] \approx 2.2$  (see Figure 12). On the other hand, oscillations do not change the nucleosynthesis very much in cases A5 and B5 despite the significant changes of  $Y_e$  (see Figure 12). This result comes about because the  $Y_e$  in these cases corresponds to a proton-rich wind that undergoes the  $\nu p$ -process similar to the case of no oscillations. We conclude that active–sterile neutrino oscillations with vacuum mixing parameters similar to those in cases A and B can greatly affect nucleosynthesis in the winds at the early epochs of  $t_{\text{pb}} \sim 1$ – $2$  s during the CCSN evolution.

In agreement with previous studies (e.g., Wu et al. 2014), we find that active–sterile neutrino oscillations near the PNS exhibit features beyond the usual MSW effect that is dominated by the potential  $V_{\text{mat}}$  from neutrino forward scattering on matter particles. These interesting features are caused by the potential  $V_\nu$  from neutrino forward scattering on other neutrinos, and more importantly, by the feedback of oscillations on both  $V_{\text{mat}}$  and  $V_\nu$  (see Figure 11). In particular, we have observed plateau-like behaviors of  $V_{\text{tot}} = V_{\text{mat}} + V_\nu$  for the outer MSW-like resonances in case C5 (see Figure 8(c)) and for the inner resonances in all the wind models with vacuum mixing parameters of cases A and B (see Figure 9). We have given only a qualitative explanation of such behaviors here, and plan to investigate them in detail in a follow-up study. In addition, we have made some simplifying approximations in our present study. For example, we have assumed that all active neutrinos are emitted from the same sharp neutrinosphere. In reality, where neutrinos decouple from matter depends on the neutrino species and energy. Although using slightly different neutrinospheres for  $\nu_e$ ,  $\bar{\nu}_e$ , and  $\nu_x$  ( $\bar{\nu}_x$ ) is more realistic, we do not expect that this modification would affect our results qualitatively. Nevertheless, we also plan to check the effects of this and other possible improvements of our model in the follow-up study.

We thank Gabriel Martínez-Pinedo for discussion during the initial phase of our study. We also acknowledge the Minnesota Supercomputing Institute at the University of Minnesota for providing resources that contributed to the research results reported here. This work was supported in part by the U.S. Department of Energy [DE-FG02-87ER40328 (UM)], the Ministry of Science and Technology of Taiwan [107-2119-M-001-038 (IOP)], the National Natural Science Foundation of China [11533006, 11655002 (TDLI)], and the Science and Technology Commission of Shanghai Municipality [16DZ2260200 (TDLI)].

### Appendix Rates of Neutron-Proton Interconversion and of Energy Gains and Losses

The rate  $\lambda_{\nu_e n}$  is given by Equation 13(b). Using the same notation, we can write  $\lambda_{\bar{\nu}_e p}$  as

$$\lambda_{\bar{\nu}_e p} = \frac{G_F^2 |V_{ud}|^2 (1 + 3g_A^2)}{2\pi^2} \frac{L_{\bar{\nu}_e} D(r)}{R_\nu^2 \langle E_{\bar{\nu}_e} \rangle} \int_{E_{\text{th}}}^{\infty} (E - \Delta)^2 \times \left(1 - \frac{W_{\bar{\nu}_e} E}{m_N}\right) f_{\bar{\nu}_e}(E) P_{\bar{\nu}_e}(E, r) dE, \quad (31)$$

where  $E_{\text{th}} = \Delta + m_e$  is the threshold  $\bar{\nu}_e$  energy for absorption on protons,  $m_e$  is the electron rest mass, and

$$W_{\bar{\nu}_e} = \frac{2[1 + 5g_A^2 + 2g_A(1 + f_2)]}{1 + 3g_A^2}. \quad (32)$$

In the above equations,  $V_{ud} = 0.974$ ,  $g_A = 1.27$ , and  $f_2 = 3.71$ . The rates  $\lambda_{e^+ n}$  and  $\lambda_{e^- p}$  are

$$\lambda_{e^+ n} = \frac{G_F^2 |V_{ud}|^2 (1 + 3g_A^2)}{2\pi^3} T^5 \left[ g_{0,2,0} \left( \frac{m_e}{T}, \eta, \frac{\Delta}{T}, 0 \right) - \frac{W_{\nu_e} T}{m_N} g_{1,2,0} \left( \frac{m_e}{T}, \eta, \frac{\Delta}{T}, 0 \right) \right], \quad (33)$$

$$\lambda_{e^- p} = \frac{G_F^2 |V_{ud}|^2 (1 + 3g_A^2)}{2\pi^3} T^5 \left[ g_{0,2,0} \left( \frac{\Delta}{T}, -\eta, -\frac{\Delta}{T}, 0 \right) - \frac{W_{\nu_e} T}{m_N} g_{1,2,0} \left( \frac{\Delta}{T}, -\eta, -\frac{\Delta}{T}, 0 \right) \right], \quad (34)$$

respectively, where  $\eta = \mu/T$ ,  $\mu$  is the electron chemical potential, and

$$g_{i,j,k}(x_{\text{th}}, y, z, w) = \int_{x_{\text{th}}}^{\infty} \frac{x^{i+1} (x+z)^j (x+w)^k \sqrt{x^2 - (m_e/T)^2}}{\exp(x+y) + 1} dx. \quad (35)$$

The rates  $\dot{q}_{\nu_e n}$  and  $\dot{q}_{\bar{\nu}_e p}$  are

$$\dot{q}_{\nu_e n} = \frac{Y_n}{m_u} \frac{G_F^2 |V_{ud}|^2 (1 + 3g_A^2)}{2\pi^2} \frac{L_{\nu_e} D(r)}{R_\nu^2 \langle E_{\nu_e} \rangle} \times \int_0^{\infty} [E + (\Delta - m_e)] (E + \Delta)^2 \times \left(1 - \frac{W_{\nu_e} E}{m_N}\right) f_{\nu_e}(E) P_{\nu_e}(E, r) dE, \quad (36)$$

$$\dot{q}_{\bar{\nu}_e p} = \frac{Y_p}{m_u} \frac{G_F^2 |V_{ud}|^2 (1 + 3g_A^2)}{2\pi^2} \frac{L_{\bar{\nu}_e} D(r)}{R_\nu^2 \langle E_{\bar{\nu}_e} \rangle} \times \int_{E_{\text{th}}}^{\infty} [E - (\Delta - m_e)] (E - \Delta)^2 \times \left(1 - \frac{W_{\bar{\nu}_e} E}{m_N}\right) f_{\bar{\nu}_e}(E) P_{\bar{\nu}_e}(E, r) dE, \quad (37)$$

respectively. The rates  $\dot{q}_{e^+ n}$  and  $\dot{q}_{e^- p}$  are

$$\dot{q}_{e^+ n} = \frac{Y_n}{m_u} \frac{G_F^2 |V_{ud}|^2 (1 + 3g_A^2)}{2\pi^3} T^6 \left[ g_{0,2,1} \left( \frac{m_e}{T}, \eta, \frac{\Delta}{T}, \frac{m_e}{T} \right) - \frac{W_{\nu_e} T}{m_N} g_{1,2,1} \left( \frac{m_e}{T}, \eta, \frac{\Delta}{T}, \frac{m_e}{T} \right) \right], \quad (38)$$

$$\dot{q}_{e^- p} = \frac{Y_p}{m_u} \frac{G_F^2 |V_{ud}|^2 (1 + 3g_A^2)}{2\pi^3} T^6 \left[ g_{0,2,1} \left( \frac{\Delta}{T}, -\eta, -\frac{\Delta}{T}, -\frac{m_e}{T} \right) - \frac{W_{\nu_e} T}{m_N} g_{1,2,1} \left( \frac{\Delta}{T}, -\eta, -\frac{\Delta}{T}, -\frac{m_e}{T} \right) \right], \quad (39)$$

respectively.

The rates given above are the most important for modeling the neutrino-driven wind, and therefore are calculated with a higher accuracy. The other rates for energy gains and losses are less important. We adopt similar estimates of these rates to those in Thompson et al. (2001) but ignore the effects of general relativity. These approximate rates are given below.

The rate  $\dot{q}_{\nu_e N}$  is

$$\dot{q}_{\nu_e N} = \frac{\kappa_n Y_n + \kappa_p Y_p}{m_u^2} \frac{G_F^2 L_{\nu_e} D(r)}{2\pi^2 R_\nu^2 \langle E_{\nu_e} \rangle} \times \int_0^{\infty} E^3 (E - 6T) f_{\nu_e}(E) P_{\nu_e}(E, r) dE, \quad (40)$$

where  $\kappa_n = \frac{1}{4}(1 + 3g_A^2)$ ,  $\kappa_p = \left(\frac{1}{2} - 2\sin^2\theta_W\right)^2 + \frac{3}{4}g_A^2$ , and  $\sin^2\theta_W = 0.231$ . The above rate can be adapted in a straightforward manner to give  $\dot{q}_{\bar{\nu}_e N}$ ,  $\dot{q}_{\nu_e N}$ , and  $\dot{q}_{\bar{\nu}_e N}$ . Note that all active neutrinos and antineutrinos of the same energy have the same cross sections for neutral-current scattering on nucleons.

The rate  $\dot{q}_{\nu_e e^\pm}$  is

$$\dot{q}_{\nu_e e^\pm} = [\Lambda_{\nu_e e^-} n_{e^-} + \Lambda_{\nu_e e^+} n_{e^+}] \frac{G_F^2 T L_{\nu_e} D(r)}{2\pi^2 \rho R_\nu^2 \langle E_{\nu_e} \rangle} \times \int_0^{\infty} E (E - 4T) f_{\nu_e}(E) P_{\nu_e}(E, r) dE, \quad (41)$$

where  $n_{e^\pm} = (T^3/\pi^2) g_{0,0,0}(m_e/T, \pm\eta, 0, 0)$  are the number densities of positrons and electrons, respectively,  $\Lambda_{\nu_e e^-} = (C_V + C_A)^2 + \frac{1}{3}(C_V - C_A)^2$ ,  $\Lambda_{\nu_e e^+} = (C_V - C_A)^2 + \frac{1}{3}(C_V + C_A)^2$ ,  $C_V = \frac{1}{2} + 2\sin^2\theta_W$ , and  $C_A = \frac{1}{2}$ . In adapting the above rate to give  $\dot{q}_{\bar{\nu}_e e^\pm}$ ,  $\dot{q}_{\nu_e e^\pm}$ , and  $\dot{q}_{\bar{\nu}_e e^\pm}$ , note that  $\Lambda_{\bar{\nu}_e e^-} = \Lambda_{\nu_e e^+}$ ,  $\Lambda_{\bar{\nu}_e e^+} = \Lambda_{\nu_e e^-}$ ,  $\Lambda_{\nu_e e^-} = (C_V + C_A - 2)^2 + \frac{1}{3}(C_V - C_A)^2$ ,  $\Lambda_{\nu_e e^+} = (C_V - C_A)^2 + \frac{1}{3}(C_V + C_A - 2)^2$ ,  $\Lambda_{\bar{\nu}_e e^-} = \Lambda_{\nu_e e^+}$ , and  $\Lambda_{\bar{\nu}_e e^+} = \Lambda_{\nu_e e^-}$ .

The rate  $\dot{q}_{\nu_e \bar{\nu}_e}$  is

$$\dot{q}_{\nu_e \bar{\nu}_e} = \frac{\Lambda_{\nu_e \bar{\nu}_e}}{\rho} \frac{G_F^2}{36\pi^3} \frac{L_{\nu_e} L_{\bar{\nu}_e} \Psi(r)}{R_\nu^4 \langle E_{\nu_e} \rangle \langle E_{\bar{\nu}_e} \rangle} \int_0^{\infty} \times \int_0^{\infty} EE' (E + E') f_{\nu_e}(E) P_{\nu_e}(E, r) f_{\bar{\nu}_e}(E') P_{\bar{\nu}_e}(E', r) dE dE', \quad (42)$$

where  $\Psi(r) = [D(r)]^4 \{[D(r)]^2 - 6D(r) + 10\}$ ,  $\Lambda_{\nu_e \bar{\nu}_e} = C_V^2 + C_A^2$ . In adapting the above rate to give  $\dot{q}_{\nu_x \bar{\nu}_x}$ , note that  $\Lambda_{\nu_x \bar{\nu}_x} = (C_V - 1)^2 + (C_A - 1)^2$ . The rate  $\dot{q}_{e^- e^+}$  is

$$\begin{aligned} \dot{q}_{e^- e^+} = & (\Lambda_{\nu_e \bar{\nu}_e} + 2\Lambda_{\nu_x \bar{\nu}_x}) \frac{2G_F^2 T^9}{9\pi^5 \rho} \\ & \times \left[ g_{1,0,0} \left( \frac{m_e}{T}, \eta, 0, 0 \right) g_{2,0,0} \left( \frac{m_e}{T}, -\eta, 0, 0 \right) \right. \\ & \left. + g_{1,0,0} \left( \frac{m_e}{T}, -\eta, 0, 0 \right) g_{2,0,0} \left( \frac{m_e}{T}, \eta, 0, 0 \right) \right]. \quad (43) \end{aligned}$$

### ORCID iDs

Zewei Xiong  <https://orcid.org/0000-0002-2385-6771>

Yong-Zhong Qian  <https://orcid.org/0000-0002-3146-2668>

### References

- Abazajian, K. N., Acero, M., Agarwalla, S., et al. 2012, arXiv:1204.5379
- Bethe, H. A., & Wilson, J. R. 1985, *ApJ*, **295**, 14
- Duncan, R. C., Shapiro, S. L., & Wasserman, I. 1986, *ApJ*, **309**, 141
- Frohlich, C., Martínez-Pinedo, G., Liebendorfer, M., et al. 2006, *PhRvL*, **96**, 142502
- Fuller, G. M., Mayle, R. W., Wilson, J. R., & Schramm, D. N. 1987, *ApJ*, **322**, 795
- Hoffman, R., Woosley, S., & Qian, Y.-Z. 1997, *ApJ*, **482**, 951
- Janka, H.-T. 2012, *ARNPS*, **62**, 407
- Malkus, A., McLaughlin, G., & Surman, R. 2016, *PhRvD*, **93**, 045021
- Martínez-Pinedo, G., Fischer, T., & Huther, L. 2014, *JPhG*, **41**, 044008
- McLaughlin, G., Fetter, J., Balantekin, A., & Fuller, G. 1999, *PhRvC*, **59**, 2873
- Meyer, B., Mathews, G., Howard, W., Woosley, S., & Hoffman, R. 1992, *ApJ*, **399**, 656
- Mikheev, S., & Smirnov, A. Y. 1985, *SvJNP*, **42**, 913
- Nunokawa, H., Peltoniemi, J. T., Rossi, A., & Valle, J. 1997, *PhRvD*, **56**, 1704
- Pllumbi, E., Tamborra, I., Wanajo, S., Janka, H.-T., & Hüdepohl, L. 2015, *ApJ*, **808**, 188
- Qian, Y.-Z., Fuller, G. M., Mathews, G. J., et al. 1993, *PhRvL*, **71**, 1965
- Qian, Y.-Z., & Woosley, S. 1996, *ApJ*, **471**, 331
- Roberts, L., Woosley, S., & Hoffman, R. 2010, *ApJ*, **722**, 954
- Sigl, G., & Raffelt, G. 1993, *NuPhB*, **406**, 423
- Takahashi, K., Witt, J., & Janka, H.-T. 1994, *A&A*, **286**, 857
- Tamborra, I., Raffelt, G. G., Hüdepohl, L., & Janka, H.-T. 2012, *JCAP*, **01**, 013
- Thompson, T. A., Burrows, A., & Meyer, B. S. 2001, *ApJ*, **562**, 887
- Timmes, F., & Arnett, D. 1999, *ApJS*, **125**, 277
- Timmes, F. X., & Swesty, F. D. 2000, *ApJS*, **126**, 501
- Wanajo, S. 2013, *ApJL*, **770**, L22
- Wanajo, S., Kajino, T., Mathews, G. J., & Otsuki, K. 2001, *ApJ*, **554**, 578
- Witt, J., Janka, H.-T., & Takahashi, K. 1994, *A&A*, **286**, 841
- Wolfenstein, L. 1978, *PhRvD*, **17**, 2369
- Woosley, S., & Baron, E. 1992, *ApJ*, **391**, 228
- Woosley, S., & Hoffman, R. D. 1992, *ApJ*, **395**, 202
- Woosley, S., Wilson, J., Mathews, G., Hoffman, R., & Meyer, B. 1994, *ApJ*, **433**, 229
- Wu, M.-R., Duan, H., & Qian, Y.-Z. 2016a, *PhLB*, **752**, 89
- Wu, M.-R., Fernández, R., Martínez-Pinedo, G., & Metzger, B. D. 2016b, *MNRAS*, **463**, 2323
- Wu, M.-R., Fischer, T., Huther, L., Martínez-Pinedo, G., & Qian, Y.-Z. 2014, *PhRvD*, **89**, 061303